Construction of Control Network for Multi-temporal LRO NAC Images Based on Matching of Lunar Impact Craters

Pengying Liu[1,2], Jiayao Wang[1,2], Xun Geng[1,2], Zhen Peng[1,2], Jin Wang[1,2,*], Haoyu Zhang[1,2]

[1] State Key Laboratory of Spatial Datum, Faculty of Geographical Science and Engineering, Henan University, Zhengzhou, China, 450046 (wangjin@henu.edu.cn);
[2] College of Geographic Sciences, Henan University, Zhengzhou, China, 450046.

Keywords: Crater Extraction, Image Matching, Control Network, Lunar South Pole.

Abstract

The Lunar South Pole (LSP) has extreme illumination, extensive shadows and weak surface texture, which greatly challenge high-precision mapping and render conventional image matching algorithms ineffective for control network construction. To solve this problem, this paper proposes a multi-temporal LRO NAC image control network construction method based on impact crater matching, leveraging their morphological stability and spatial consistency. A manually annotated 1 m/pixel LRO NAC dataset was used to train YOLOv8 for accurate crater parameter extraction. A virtual feature point matching algorithm was developed, which builds crater descriptors by fusing geometric attributes and neighborhood topology, and achieves reliable matching via multi-attribute similarity and bidirectional verification. Secondary NCC refinement was applied to large craters to improve tie point accuracy. Finally, tie points were mapped back to original images for control network construction and bundle adjustment. Comparative experiments on 94 LRO NAC images near 88.5°S (2298 pairs) with SIFT and SuperPoint showed that the proposed method generated ~10,000 stable tie points per pair, with only 45 pairs lacking valid tie points—far fewer than the comparison algorithms. A large-area control network built from 1,847 images yielded 2,219,604 tie points. After bundle adjustment, the unit weight standard error was 0.67, average image RMS 0.83 pixels, maximum below 2 pixels. The resulting DOM and DEM products had excellent quality. This method effectively solves the LSP tie point matching problem and supports high-precision lunar polar topographic mapping.

1. Introduction

The Lunar South Pole (LSP) is highly significant for deep space resource utilization and scientific research due to its unique environment and spatial location. However, mapping in the LSP faces great challenges from its distinctive environment, such as drastic shadow changes and rugged terrain. A crucial prerequisite for high-precision mapping of the LSP is constructing a high-quality control network, with image matching being a key issue in establishing such a network (Chen, C., et al., 2024; Liu, P.Y., et al., 2024). The LSP's unique environment poses substantial challenges to conventional image matching algorithms, which often require specific optimization to achieve stable matching.

One of the critical issues in lunar south pole cartography is image matching. The special environmental conditions at the lunar south pole pose substantial challenges to conventional image matching algorithms, which typically require targeted optimization and modification to achieve stable image matching in this region. As an important interdisciplinary algorithm, image matching is widely applied in computer vision, photogrammetric mapping, 3D reconstruction, and other fields. With the rapid advancement of these disciplines, image matching plays an indispensable role in numerous application domains.Traditional image matching methods are mainly categorized into intensity-based matching and feature-point-based matching. Among them, feature-point-based matching demonstrates favorable stability and strong robustness to image scaling, rotation, and illumination variations, thereby emerging as the mainstream approach in image matching.

Feature extraction and description constitute the core of image matching algorithms, and relevant research has been conducted for a long time. In 2004, Lowe et al. first proposed the Scale-Invariant Feature Transform (SIFT) algorithm (Lowe, D.G., 2004), which constructs a linear pyramid scale space using difference-of-Gaussian kernels and extracts scale-invariant extrema from it, followed by generating 128-dimensional descriptors via image gradient histograms. Nevertheless, the high computational complexity of SIFT results in relatively low matching efficiency. To address this limitation, Bay et al. introduced the Speeded Up Robust Features (SURF) algorithm in 2006 (Bay, H., et al., 2008). This algorithm improves SIFT by employing box-type filters to simplify the Gaussian scale space, reduces the descriptor dimension from 128 to 64 while preserving robustness, and thus enhances matching efficiency. In 2011, Rublee et al. modified the Features from Accelerated Segment Test (FAST) detector and Binary Robust Independent Elementary Features (BRIEF) descriptor, proposing the Oriented FAST and Rotated BRIEF (ORB) algorithm (Rublee, E., et al., 2011). This method adopts binary feature vectors and realizes fast image matching using Hamming distance. Experimental results validate that the matching speed of ORB is over ten times faster than those of SURF and SIFT.

In addition to these classic feature-point algorithms, extensive research has been devoted to developing improved variants. In 2017, Mur-Artal et al. first integrated a quadtree distribution algorithm into their proposed ORB-SLAM (Simultaneous Localization and Mapping) framework to mitigate the dense clustering of feature points, eliminating mismatches caused by feature aggregation and enabling the feature-point matching algorithm to meet the requirements of visual SLAM (Mur-Artal, R., et al., 2017). Based on the SURF algorithm, Chum proposed an enhanced scheme incorporating the PROgressive SAmple Consensus (PROSAC) algorithm for outlier rejection, which strengthens the stability of feature extraction and improves matching accuracy (Chum, O., et al., 2005). Starting from

* Corresponding author

https://doi.org/10.5194/isprs-archives-XLIX-B2-2026-467-2026

threshold optimization, Dai et al. improved the ORB algorithm by combining image enhancement with truncated adaptive thresholds to accommodate feature extraction from diverse images under varying conditions (Dai, Y., et al., 2023). In 2022, Tan et al. embedded the Grid-based Motion Statistics (GMS) algorithm into ORB, extracting feature points uniformly via quadtree allocation and removing mismatches with GMS validation, yielding superior extraction and matching performance over the original ORB algorithm (Tan, Z., et al., 2023).

In recent years, deep learning has significantly influenced image matching. Traditional methods rely on handcrafted features (e.g., SIFT, SURF) and exhibit significant performance degradation in challenging scenarios such as weak texture and substantial illumination variations. CNN-based deep learning models (e.g., SuperPoint, LoFTR) enable higher-level semantic representation through end-to-end feature learning (DeTone, D., et al., 2018; Sun, J.M., et al., 2021). Recent advances have also been achieved in lunar image matching, particularly for the lunar south pole. Owing to extreme illumination conditions, extensive shadow coverage, and texture scarcity in lunar images, traditional algorithms face severe challenges. Taking the lunar south pole as an example, its permanently shadowed regions lack continuous textures, and the extremely low solar elevation angle results in weak image contrast, leading to poor performance of conventional feature point extraction and matching. To address the weak-texture problem in the lunar south pole, Tong Xiaohua's team proposed a stereo matching algorithm based on confidence evaluation. By constructing a triangulated mesh and dynamically updating the set of support points, experiments on LRO NAC images over the Shackleton Crater in the south pole showed that the matching accuracy was improved by 30% compared with the traditional Semi-Global Matching (SGM) method, and the elevation consistency with LOLA DEM data reached 95%. In terms of multimodal image matching, Di Kaichang's team targeted the radiometric differences between optical and SAR images by constructing feature vectors using anisotropic filtering and Histogram of Absolute Phase Consistency Gradients (HAPCG). This method achieved a matching accuracy of 78% for shadowed regions in the lunar south pole, significantly outperforming traditional SIFT and LoFTR algorithms. Lunar south pole craters serve as ideal feature points due to their morphological stability. A virtual control network construction method based on the spatial distribution pattern of craters extracts crater centers as feature points and optimizes matching results with geometric constraints, enabling sub-pixel localization accuracy in low-overlap images (Li, Y., et al., 2024). In 2024, a research team from Shenzhen University introduced camera ray matching into neural radiance field reconstruction, jointly optimizing camera poses and scene representation. For lunar surface images in low-texture regions, the novel view synthesis error was reduced by 42% compared with the traditional NeRF (Neural Radiance Fields) (Lin, L., et al., 2024).

Deep learning techniques have also achieved remarkable progress in the field of feature recognition, demonstrating powerful capabilities, especially in tasks such as image semantic segmentation and object detection. CNN-based models, including U-Net (Convolutional Networks for Biomedical Image Segmentation) and the YOLO series, have significantly improved the accuracy and robustness of crater detection through multi-scale feature fusion and adaptive learning mechanisms (DeLatte, D.M., et al., 2019). Traditional crater detection methods rely on handcrafted features such as edge detection and ellipse fitting, which are susceptible to noise interference in complex terrains. In contrast, deep learning-based detection algorithms realize end-to-end feature learning and substantially enhance the ability to identify multi-scale craters. For instance, the dense point crater detection network designed by Chen et al. optimizes detection speed via a lightweight network architecture, achieving an average recognition accuracy of 98.5% (Chen, Z., et al., 2021). Nevertheless, the low signal-to-noise ratio caused by permanently shadowed regions in the south polar area still poses challenges to the generalization ability of detection models.

The dense distribution and stable geometric relationships of craters in the south polar terrain provide natural constraints for matching algorithms. Fusing geometric descriptors with regional gradient features can effectively improve matching robustness. Jin et al. constructed a geometric configuration graph and combined geometric descriptors based on Delaunay triangulation with normalized regional gradient features to generate scale-invariant composite descriptors, achieving a matching accuracy of over 90% under rotation and illumination variations (Jin, M., et al., 2024). Yang et al. proposed a coarse-to-fine matching strategy: after screening candidate regions using the Hausdorff distance, mismatches were eliminated via an affine transformation model constrained by mutual information, with an average positioning error of less than 3 pixels, significantly improving matching stability in high-latitude regions (Yang, Z., et al., 2023). Qian et al. constructed affine-invariant descriptors using the angles and side-length ratios of crater triangles. Based on rigid transformation and reprojection error, their matching method realized high-precision matching under 10:1 resolution differences by dynamically adjusting affine parameters (Qian, Z., et al., 2022). Fairweather et al. combined the YOLOv3 detection model with dynamic threshold segmentation, achieving a matching accuracy of 93% for craters smaller than 20 meters in diameter, which verified the applicability under complex illumination conditions in the south polar region (Fairweather, J.H., et al., 2022).

However, lunar polar images—characterized by extreme illumination conditions, extensive shadows, and weak texture pose significant challenges to both handcrafted and deep learning methods. The permanent shadow regions (PSRs) in the lunar polar regions lack continuous texture, while extremely low solar elevation severely reduces image contrast. Though certain deep learning methods have been applied, most have been developed and evaluated primarily on mid- and low-latitude imagery, leaving their generalization capability and robustness under extreme polar illumination conditions insufficiently explored.

2. Control Network Construction Based on Lunar Impact Craters Matching

Impact craters are a prominent and stable feature in the LSP (Liu, S., et al., 2025). This paper presents a crater matching algorithm based on YOLOv8 object detection (Redmon, J., et al., 2016), which exploits the morphological stability and spatial consistency of impact craters. The algorithm utilizes a self-constructed dataset of LRO (Lunar Reconnaissance Orbiter) NAC (Narrow Angle Camera) images. Following crater detection, geometric relationships between each crater and its neighbouring craters are systematically established. Key attributes including crater coordinates, size, inter-crater distance, and azimuth angle are integrated to form comprehensive descriptors of craters. These descriptors are then used to match corresponding "virtual" feature points in LRO NAC images in the lunar polar regions. Figure 1 shows the network architecture of YOLOv8.

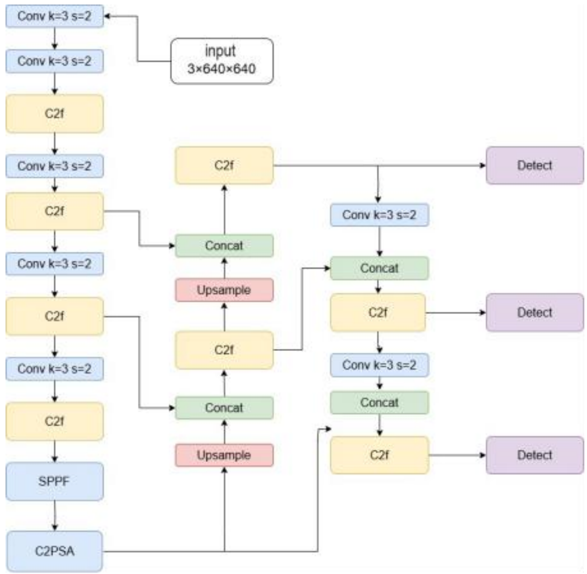

Figure 1. YOLOv8 Network Structure.

2.1 Crater Detection

This paper manually annotated LRO NAC images in the LSP to construct a dedicated dataset for targeted training of the YOLO network, enabling accurate crater identification. The images used for dataset construction are multi-temporal orthophotos with a resolution of 1 meter/pixel derived from LRO NAC images, comprising a total of 94 images. Approximately 70% of the annotated images were allocated for training, while the remaining 30% were reserved for validation of the model performance. Based on the trained model, the pixel coordinates of the crater centers and the crater dimensions represented by semi-major and semi-minor axes can be reliably extracted. A representative result of crater detection is shown in Figure 2.

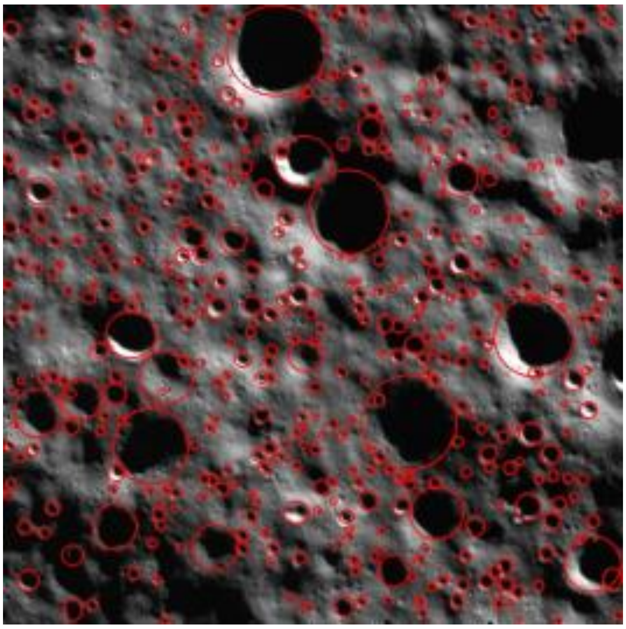

Figure 2. Example of Crater Detection Results.

2.2 Virtual Feature Point Matching Based on the Semantic Information of Lunar Impact Craters

The workflow of virtual feature point matching based on the semantic information of impact craters is shown in Figure 3.

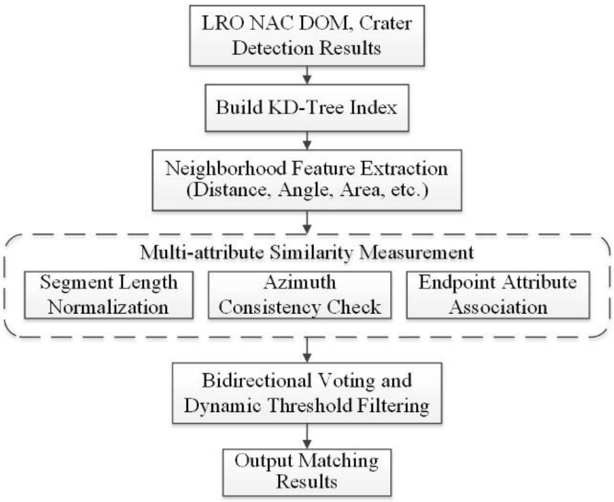

Figure 3. Workflow of virtual feature point matching based on the semantic information of lunar impact craters.

The proposed method constructs local feature descriptors by integrating the geometric attributes of craters (e.g., coordinates, aspect ratio) and the topological relationships among neighboring impact craters. The underlying principle is that the geometric attributes of a given crater and its spatial configuration relative to surrounding impact craters must satisfy consistency constraints such as inter-crater distance, azimuth angle, and aspect ratio. Consequently, corresponding craters detected in multiple images can be reliably matched and utilized as virtual feature points. Figure 4 shows a schematic illustration of crater neighborhood matching.

The specific process comprises the following six procedural steps:

1. Crater Detection: Detect lunar impact craters on the LRO NAC images using the trained YOLOv8 model. Then, perform coordinates conversion from pixel coordinates to geographic coordinates (i.e., map projection coordinates).
2. Spatial Index Construction: Partition the detected impact craters spatially according to their geographic coordinates using a KD-tree (K-dimensional Tree) structure to accelerate efficient neighborhood queries.
3. Neighborhood Feature Extraction: Dynamically determine the search radius for each impact crater to identify its neighboring craters within the local vicinity. Compute topographic relationships among neighboring impact craters, such as the inter-crater distance and azimuth angle of the line connecting the centers of two impact craters.

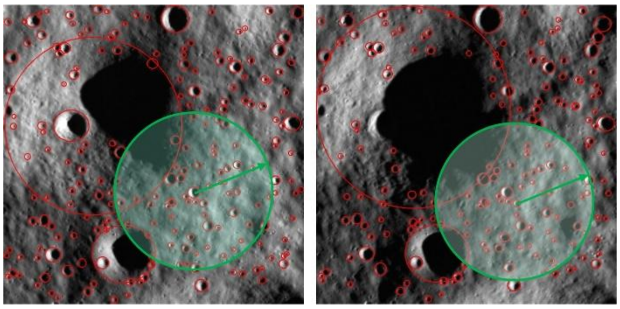

Figure 4. Diagram of Impact Crater Matching based on Neighborhood Search.

4. Similarity Measurement: Calculate the matching probability through a multi-attribute weighted model that integrates geometric and morphological features.
5. Bidirectional Verification and Filtering: Apply a bidirectional voting mechanism to eliminate mismatched pairs, ensuring

mutual correspondence between candidate matches and significantly reducing false positives.

6. Result Output: Generate output files containing matched impact crater pairs and provide visual visualization of the successfully matched virtual feature points.

2.3 Control Network Construction

The illumination conditions in the LSP vary significantly, resulting in widespread and dynamic shadow distribution. This leads to significant differences in the appearance of shadows associated with the same impact crater across multi-temporal images. As a result, the detection accuracy is adversely affected, causing positional deviations in the identified locations of corresponding impact craters under different illumination conditions. This effect is particularly pronounced for larger craters. To ensure reliability, only small-sized impact craters with high detection consistency were used for constructing the control network and supporting subsequent processing steps. For larger craters, where slight detection inaccuracies may propagate into tie points misalignments, a further refinement procedure was implemented. This process used the initially detected crater center as a seed point for secondary matching by the classic normalized cross-correlation (NCC) matching method, thereby improving the accuracy of virtual tie points for large-sized impact craters.

Crater detection was conducted in the orthophoto space derived from the original images, which effectively reduces mismatches caused by topographic deformation and enhances matching stability. After the matching process is completed, a series of coordinate transformations are applied to map the initial tie points back to the original image space for subsequent control network construction. These transformations specifically involve converting the impact crater centers from orthophoto pixel coordinates to original image pixel coordinates through back-projection from ground coordinates to image coordinates (Geng, X., et al., 2019). Once these steps are finalized, the control network can be constructed by merging all matched pairs.

3. Experiments and Results

To validate the reliability and effectiveness of the proposed method, two sets of experiments were conducted. The experiments conducted a comparative test between our method and the traditional SIFT and SuperPoint methods. The results demonstrated that the proposed method performed better for images in the lunar polar regions.

3.1 Comparison of Image Matching Algorithms

3.1.1 Image Matching Dataset

The experiment selected 94 images near latitude 88.5°S at the Lunar South Pole, resulting in 2298 image pairs with overlapping relationships. By analyzing the matching results of these 2298 pairs, the performance differences with other matching methods were compared. Regarding illumination differences in the images, Figure 5 shows three examples from all matching pairs, respectively illustrating the overlapping relationships and image detail comparisons for image pairs with large, medium, and small illumination differences.

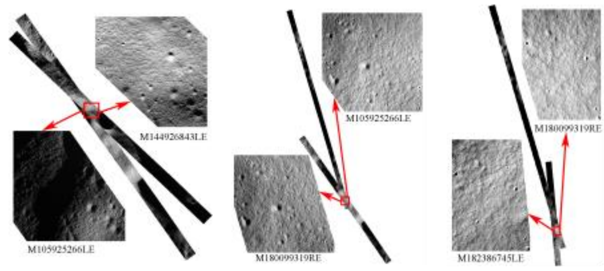

a. Large Difference b. Medium Difference c. Small Difference

Figure 5. Overlaps of Image Pairs for Comparison Experiment.

3.1.2 Matching Results

SuperPoint is a self-supervised matching algorithm based on deep learning. Feature extraction is performed using SuperPoint, and matching is completed with SuperGlue (collectively referred to as SuperPoint hereinafter). SIFT is a classic feature extraction and matching algorithm, which implements matching based on 128-dimensional feature descriptors. In the experiment, all results of the 2,298 matching pairs under crater matching, SuperPoint matching, and SIFT matching were statistically analyzed. For SuperPoint, the matching parameters were set as a detection threshold of 0.005, a matching threshold of 0.2, and a maximum number of detected feature points of 10000; for SIFT, the block size was 256×256, with 50000 feature points extracted from each block for matching.

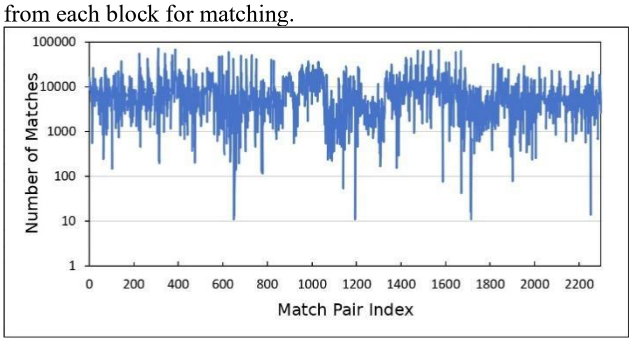

a. Crater matching results

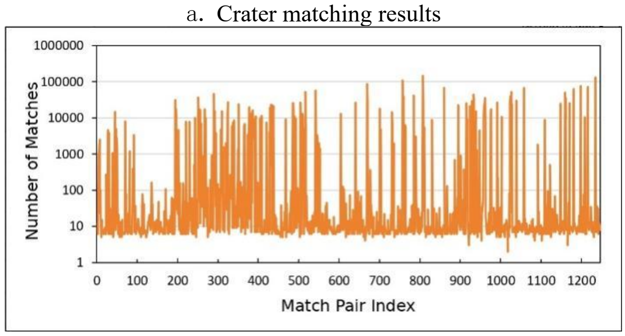

b. SuperPoint matching results

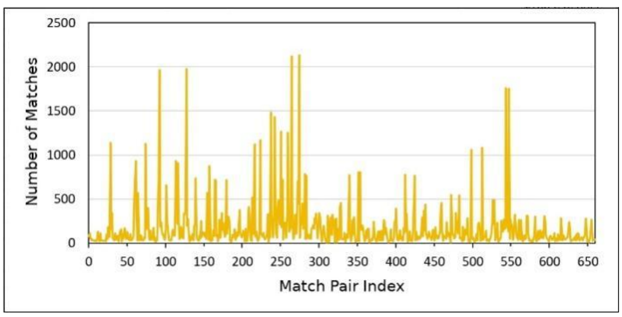

c. SIFT matching results

Figure 6. Statistics of matching results.

The statistical results of the matching performance are shown in Figure 6. In the crater matching results, the number of matching correspondences is approximately 10000; most SuperPoint matching results yield fewer than 100 matching points, while most SIFT matching results have fewer than 500 matching points. Additionally, the number of matching points obtained by the other two matching methods exhibits significant fluctuations.

3.1.3 Results Statistics and Analysis

Furthermore, the experiment also statistically analyzed the distribution intervals of matching point counts for the three methods. The specific statistical results are presented in Table 1. It can be observed that the point counts of crater matching are mainly distributed in two intervals: 1000–10000 and 10000–100000. The point counts of SuperPoint matching are concentrated in three intervals: 1–50, 1000 - 10000, and 10000–100000. For SIFT matching, the point counts predominantly fall within the intervals of 1–50 and 100–1000. Among all matching pairs of crater matching, only 45 pairs have no corresponding matching points; in contrast, SuperPoint and SIFT fail to obtain matching correspondences for 1052 and 1638 matching pairs respectively.

Range of Matched Points	Crater Matching (Number of Pairs)	SuperPoint (Number of Pairs)	SIFT (Number of Pairs)
Greater than 100,000	0	3	0
10,000~100,000	562	85	0
1,000~10,000	1,533	82	16
100~1000	148	50	276
50~100	3	53	159
1~50	7	973	209
No Matched Points	45	1,052	1,638

Table 1. Statistics on the Distribution of Matched Point Counts.

Overall, SuperPoint is most susceptible to the size of image overlapping areas and illumination differences. Nevertheless, it can still match a small number of low-confidence points even under conditions of small overlapping areas. When the overlapping area is large, SIFT yields fewer matching points than SuperPoint, and it cannot perform effective matching when the overlapping area is excessively small. In comparison, crater matching demonstrates stable performance; it can achieve reliable matching even for small overlapping areas, and its matching result is only related to the number of impact craters within the overlapping region.

3.2 Control Network Construction for Large-scale LRO NAC Images

The experiment utilized 1,847 LRO NAC images to construct a large-area control network. The distribution of the tie points was shown in Figure 11. As can be seen, even in the extremely dark and shadowed regions in the LSP, where light conditions are very poor, the proposed method can still obtain a sufficient number of tie points. Based on the derived control network, the bundle adjustment yielded a $\sigma 0$ of 0.67. The bundle adjustment results for large-scale LRO NAC images are shown in Table 2.

3.2.1 Basic Information of the Dataset

For the dataset adopted in crater matching and control network construction, this paper statistically analyzes its basic information, including the solar incidence angle and azimuth angle (illumination conditions), as well as the detector emission angle and azimuth angle (imaging observation conditions). Moreover, the distribution relationships of the incidence angles, emission angles, and azimuth angles are intuitively presented in the form of polar coordinate diagrams.

It can be seen from Figure 7 that the solar incident angles are mainly distributed between 60∘ and 80∘, corresponding to elevation angles ranging from 20∘ to 30∘; the azimuth angles show a semicircular distribution. This is because the dataset covers the area between 60∘S and 75∘S in the southern hemisphere. Due to the axial tilt of the Moon, the solar azimuth is basically confined within a 180∘ range, and an all-round 360∘ azimuth distribution only appears near the lunar polar regions. As shown in Figure 8, apart from a few slightly large emission angles, most emission angles are single-digit values, and the azimuth angles are distributed over the full 360∘ range.

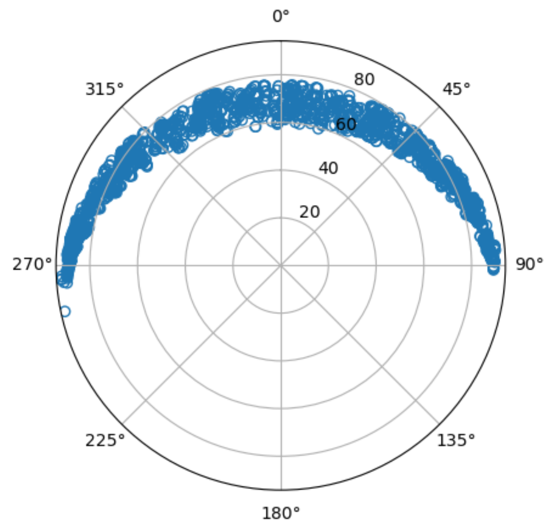

Figure 7. Distribution of illumination incidence angle and azimuth angle.

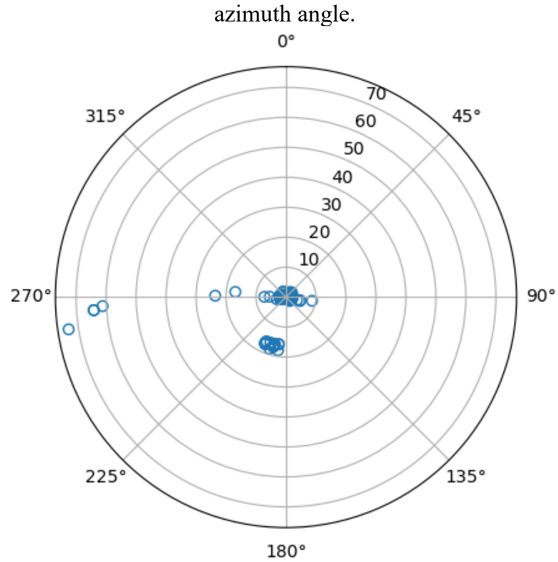

Figure 8. Distribution of spacecraft emission angle and azimuth angle.

3.2.2 Analysis of Crater Matching Results

Reliable crater matching results serve as an essential prerequisite for control network construction, especially for large-area control network establishment and mapping tasks. Most traditional feature matching algorithms and emerging methods (including

https://doi.org/10.5194/isprs-archives-XLIX-B2-2026-467-2026

deep learning-based matching algorithms) struggle to cope with lunar south pole images suffering from extreme illumination differences. In other words, for image pairs with large variations in illumination angles, the obtained tie points are unstable. This issue is fatal to high-precision large-area control network construction, which greatly degrades the control network accuracy, image stitching quality, and also affects the image exterior orientation parameters and subsequent terrain reconstruction.

As relatively stable geometric landforms, impact craters can be adopted as virtual tie points to effectively address the above problem. Figure 9 shows a stereo image pair with a huge difference of 90° in illumination azimuth angles between the two frames within this small coverage area. Nevertheless, the two images are successfully connected via crater matching.

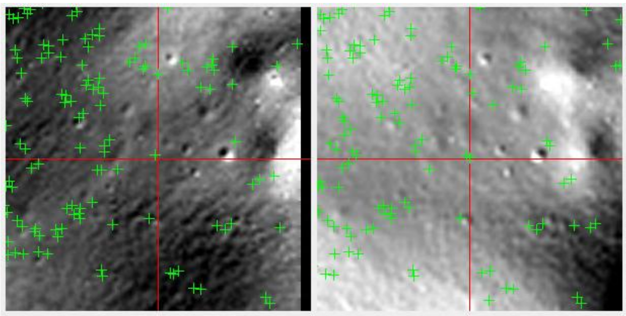

Figure 9. Image matching results for pairs with large illumination differences (Green crosshairs denote matched tie points; red crosshairs represent current tie points; the images are downsampled to 1/20 of the original resolution).

Figure 10 presents another crater matching example for a stereo pair. This stereo pair has an extremely small overlapping area, accounting for only a few tenths of the entire NAC image, accompanied by significant illumination differences. Even so, the proposed crater matching algorithm obtains more than 5000 tie points.

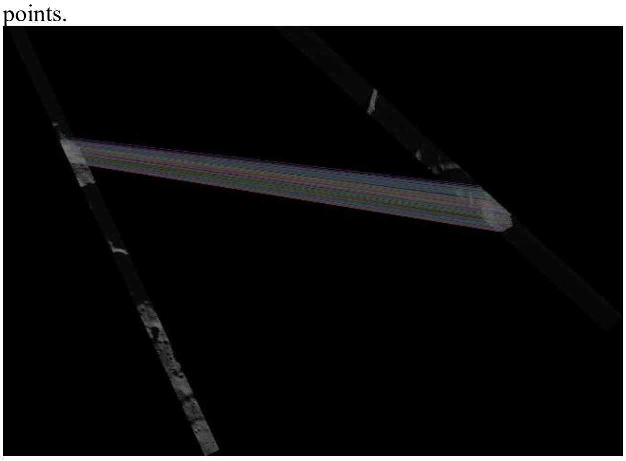

Figure 10. Crater matching results for small-area matching pairs.

3.2.3 Construction Results and Accuracy Analysis of Control Network

The control network constructed from crater matching results is shown in Figure 11. It can be seen that the tie points are distributed very uniformly and almost cover the entire mapping area. The 109 uniformly distributed purple crosshairs represent elevation control points derived from the LOLA DEM. A certain threshold is assigned to these points to ensure that the entire control network does not deviate excessively during bundle adjustment, thereby anchoring its basic position.

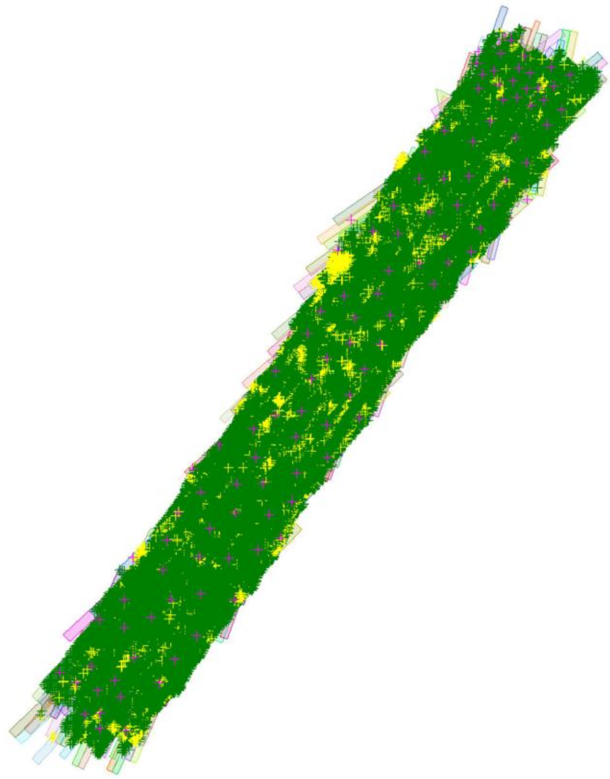

Figure 11. Distribution of Tie Points (Green crosshairs indicate valid tie points, yellow crosshairs indicate invalid tie points, and purple crosshairs indicate elevation control points from LOLA).

Figure 12 statistically presents the measure counts of all tie points in the control network, where the maximum measure count reaches 23. Tie points with a measure count of no less than 3 account for nearly 70%, and those with a measure count of no less than 4 exceed 50%. A higher measure count of tie points indicates tighter interconnection among images in the constructed control network, as well as better stability and higher accuracy of the control network.

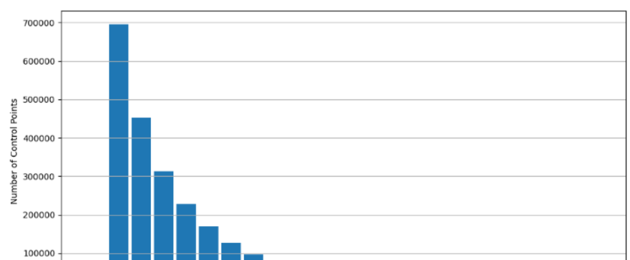

Figure 12. Histogram of tie point measure quantity distribution.

The control network consists of 1,847 LRO NAC images, 2,219,604 tie points, and 9,158,758 measurement points. After bundle adjustment, the unit weight standard error $\sigma 0$ reaches 0.67. Figure 13 shows the statistics of the RMS values of all images, with an average of 0.83 and a standard deviation of 0.22. It can be observed that the maximum RMS value is no more than 2 pixels, and most values are below 1.25 pixels.

Table 2. Statistics of Bundle Adjustment.

Metric	Parameter
Number of Images	1,847
Number of Tie Points	2,219,604
Number of Measurements	9,158,758
Sigma0	0.67

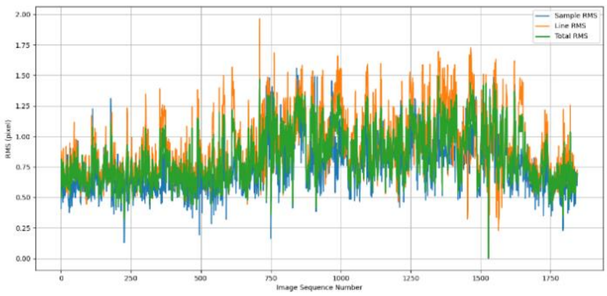

Figure 13. Image RMS Line Chart.

3.2.4 Mapping Results

Mapping accuracy is the most direct indicator for evaluating the quality of control networks and bundle adjustment. Block bundle adjustment aims to eliminate errors among images acquired at different times and in different regions, and refine the exterior orientation parameters of images. Since the exterior orientation parameters of images are required for DOM generation and DEM terrain reconstruction, DOM and DEM products can inherently verify the pose errors between images.

a. Maximum mosaic.

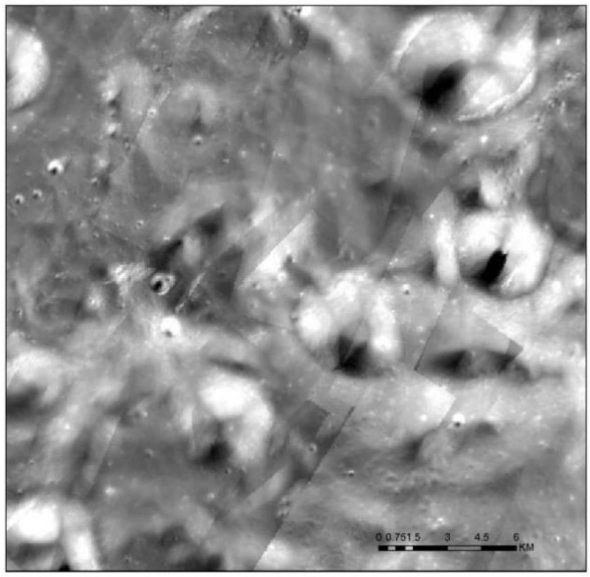

b. Local stitching effect.
Figure 14. DOM mosaic image.

As shown in Figure 14, (a) presents the global maximum mosaic of DOM generated from all 1,847 images in the mapping area after updating exterior orientation parameters via bundle adjustment; (b) shows the local stitching effect. Faint boundaries between adjacent images can be observed, yet the stitching quality of impact craters and lunar surface terrain is excellent.

Figure 15 illustrates the terrain reconstruction results by the SfS method for a 25 km × 25 km area within the mapping region. Subplot (a) is the currently highest-resolution LOLA DEM product (60 m/pixel) of this area, and (b) is the SfS DEM product (30 m/pixel) generated by the proposed method. The comparison indicates that the SfS terrain reconstruction achieves favorable performance. Compared with the LOLA DEM, it eliminates striping artifacts caused by original laser point differences, delivers finer terrain details, and recovers numerous smaller impact craters that are absent in the LOLA DEM.

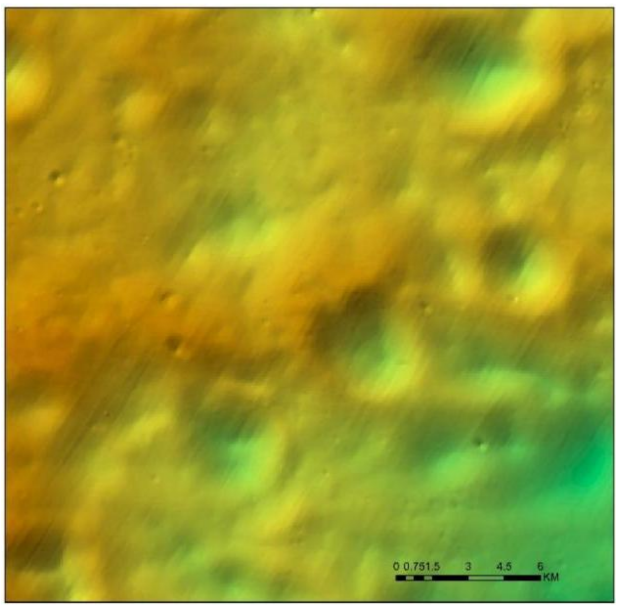

a. LOLA DEM (60 m/pixel).

https://doi.org/10.5194/isprs-archives-XLIX-B2-2026-467-2026 |

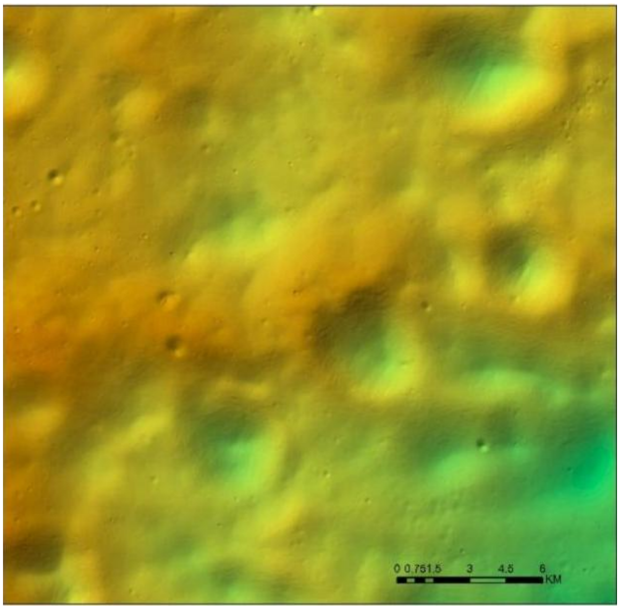

b. SfS DEM from the control network constructed by the proposed method (30 m/pixel).
Figure 15. Rendered DEM maps.

4. Conclusion and Discussion

The experimental results based on two sets of LRO NAC images demonstrate that the proposed method can generate stable and abundant tie points from lunar polar images, outperforming conventional SIFT and SuperPoint matching algorithms. By leveraging the semantic information of the lunar impact craters, the proposed method is well suited for processing lunar polar images characterized by weak texture and significant illumination variations. Consequently, it enables the automatic construction of a high-quality control network for thousands of multi-temporal LRO NAC images in the LSP. It will have great potential for application in the derivation of high-accuracy topographic maps in the lunar polar regions.

Acknowledgements

This work was supported by the State Key Laboratory of Spatial Datum under grant SKLSD2025-ZZ-13; the National Natural Science Foundation of China under Grant 42241147; the Space Optoelectronic Measurement and Perception Lab, Beijing Institute of Control Engineering under Grant LabSOMP-2023-07. (Corresponding author: Xun Geng.)

References

Bay, H., Tuytelaars, T., Van Gool, L.S., 2008: Speeded Up Robust Features (SURF). Computer Vision and Image Understanding, 110(3), 346-359.

Chen, C., Ye, Z., Xu, Y., et al., 2024: Large-Scale Block Bundle Adjustment of LROC NAC Images for LSP Mapping Based on Topographic Constraint. IEEE Journal of Selected Topics in Applied Earth Observations and Remote Sensing, 17, 2731-2746. doi.org/10.1109/JSTARS.2023.3346199.

Chen, Z., Jiang, J., 2021: Crater detection and recognition method for pose estimation. Remote Sensing, 13: 3467.

Chum, O., Matas, J., 2005: Matching with PROSAC - progressive sample consensus. 2005 IEEE Computer Society Conference on Computer Vision and Pattern Recognition, San Diego, USA, 1, 220-226.

Dai, Y., Wu, J., 2023: An Improved ORB Feature Extraction Algorithm Based on Enhanced Image and Truncated Adaptive Threshold. IEEE Access, 11: 32073-32081.

DeLatte, D.M., Crites, S.T., Guttenberg, N., et al., 2019: Segmentation convolutional neural networks for automatic crater detection on mars. IEEE Journal of Selected Topics in Applied Earth Observations and Remote Sensing, 12(8): 2944-2957.

DeTone, D., Malisiewicz, T., Rabinovich, A., 2018: SuperPoint: Self-Supervised Interest Point Detection and Description. 2018 IEEE/CVF Conference on Computer Vision and Pattern Recognition Workshops, Salt Lake City, USA, 337-33712.

Fairweather, J.H., Lagain, A., Servis, K., et al., 2022: Automatic mapping of small lunar impact craters using LRO-NAC images. Earth and Space Science, 9: e2021EA002177.

Geng, X., Xu, Q., Xing, S., et al., 2019: A Robust Ground-to-Image Transformation Algorithm and Its Applications in the Geometric Processing of Linear Pushbroom Images. Earth and Space Science, 6(10): 1805-1830.

Jin, M., Shao, W., 2024: Crater Triangle Matching Algorithm Based on Fused Geometric and Regional Features. Aerospace, 11: 417.

Li, Y., Zeng, Y., 2024: Lunar Image Matching Based on Impact Crater Morphology and Distribution for Landing Localization. 2024 IEEE International Geoscience and Remote Sensing Symposium, Athens, Greece, 6146-6149.

Lin, L., Wu, W., Fu, C.W., et al., 2024: CRAYM: Neural Field Optimization via Camera Ray Matching. Conference on Neural Information Processing Systems.

Liu, P.Y., Geng, X., Li, T., Zhang, J.J., Ma, X., et al., 2024: The Generation of High-Resolution Mapping Products for the LSP Using Photogrammetry and Photoclinometry. Remote Sensing, 16(12): 2097.

Liu, S., Chu, G., Xu, C., et al., 2025: Lunar Crater Matching With Triangle-Based Global Second-Order Similarity for Precision Navigation. IEEE Transactions on Geoscience and Remote Sensing, 63: 1-17. doi.org/10.1109/TGRS.2025.3598104.

Lowe, D.G., 2004: Distinctive Image Features from Scale-Invariant Keypoint. International Journal of Computer Vision, 60(2): 91-110.

Mur-Artal, R., Montiel, J.M., 2017: ORB-SLAM: A Versatile and Accurate Monocular SLAM System. IEEE Transactions on Robotics, 33(5): 1147-1163.

Qian, Z., Cheng, H., Hu, T., et al., 2022: A New Approach Based on Crater Detection and Matching for Self-Localization During Lunar Landings. The International Conference on Image, Vision and Intelligent Systems (ICIVIS 2021), Singapore, 813: 849-859.

Redmon, J., Divvala, S., Girshick, R., et al., 2016: You Only Look Once: Unified, Real-Time Object Detection. 2016 IEEE Conference on Computer Vision and Pattern Recognition (CVPR), Las Vegas, USA, 779-788.

Rublee, E., Rabaud, V., Konolige, K., et al., 2011: ORB: An effi cient alternative to SIFT or SURF. 2011 International Conferenc e on Computer Vision, Barcelona, Spain, 2564-2571.

Sun, J.M., Shen, Z.H., Wang, Y., et al., 2021: LoFTR: Detector-Free Local Feature Matching With Transformers. 2021 IEEE/C VF Conference on Computer Vision and Pattern Recognition (C VPR), 8918-8927.

Tan, Z., Fan, W., Kong, W., et al., 2023: An improved ORB-GM S image feature extraction and matching algorithm. 2023 IEEE I nternational Conference on Robotics and Biomimetics, Koh Sam ui, Thailand, 1-6.

Yang, Z., Kang, Z., Cao, Z., et al., 2023: Coarse-to-Fine Crater Matching From Heterogeneous Surfaces of LROC NAC and Ch ang'e-2 DOM Images. IEEE Geoscience and Remote Sensing Le tters, 20: 1-5.